Collective temperature anisotropy instabilities in intense charged particle beams[a)]

Edward A. Startsev,[b)] Ronald C. Davidson, and Hong Qin
Plasma Physics Laboratory, Princeton University, Princeton, New Jersey 08543

(Received 9 November 2006; accepted 12 December 2006; published online 22 March 2007)

The classical electrostatic Harris instability and the electromagnetic Weibel instability, both driven by a large temperature anisotropy $(T_{\parallel b}/T_{\perp b} \ll 1)$ that develops naturally in accelerators, are generalized to the case of a one-component intense charged particle beam with anisotropic temperature, including the important effects of finite transverse geometry and beam space-charge. Such instabilities may lead to an increase in the longitudinal velocity spread, which makes focusing the beam difficult, and may impose a limit on the beam luminosity and the minimum spot size achievable in focusing experiments. This paper describes recent advances in the theory and simulation of collective instabilities in intense charged particle beams caused by large temperature anisotropy. The new simulation tools that have been developed to study these instabilities are also described. Results of the investigations that identify the instability growth rates, levels of saturations, and conditions for quiescent beam propagation are also discussed. © *2007 American Institute of Physics*. [DOI: 10.1063/1.2436847]

I. INTRODUCTION

Periodic focusing accelerators, transport systems, and storage rings[1–3] have a wide range of applications ranging from basic scientific research in high energy and nuclear physics, to applications such as ion-beam-driven high energy density physics and fusion, and spallation neutron sources. Of particular importance at the high beam currents and charge densities of practical interest are the effects of the intense self-fields produced by the beam space charge and current on determining the detailed equilibrium, stability, and transport properties. Charged particle beams confined by external focusing fields represent an example of non-neutral plasma.[4] A characteristic feature of such plasmas is the nonuniformity of the equilibrium density profiles and the nonlinearity of the self-fields, which makes detailed analytical investigation difficult. The development and application of advanced numerical tools such as eigenmode codes[5–7] and Monte-Carlo particle simulation methods[8–13] are often the only tractable approach to understand the underlying physics of different instabilities familiar in electrically neutral plasmas. Two such instabilities are the electrostatic Harris instability[5,6,8,9,11,14] and the electromagnetic Weibel instability,[7,15] both driven by a large temperature anisotropy that develops naturally in accelerators. The beam acceleration causes a large reduction in the longitudinal temperature. Indeed, for particles with charge e_b and mass m_b accelerated by a voltage V (here i denotes the initial state before acceleration, and f denotes the state after acceleration), the energy spread of particles in the beam does not change, and (nonrelativistically) $\Delta E_{bi}=m_b\Delta v_{bi}^2/2=\Delta E_{bf}=m_bV_b\Delta v_{bf}$, where $V_b=(2e_bV/m_b)^{1/2}$ is the average beam velocity after acceleration. Therefore, the velocity spread-squared, or equivalently, the effective temperature, changes according to (for a nonrelativistic beam) $T_{\parallel bf}=T_{\parallel bi}(T_{\parallel bi}/2e_bV)$. For particles accelerated to highly relativistic energies $(\gamma_b \gg 1)$, $T_{\parallel bi}=(\Delta p_{\parallel b})_i^2/2m_b=c(\Delta p_{\parallel b}^L)_f=c\gamma_b(\Delta p_{\parallel b}^B)_f$, where L and B denote laboratory and beam-frame quantities, respectively. The longitudinal temperature is proportional to momentum-spread-squared in the beam frame, $T_{\parallel bf}=(T_{\parallel bi}/m_bc^2\gamma_b^2)T_{\parallel bi}$, whereas the transverse temperature remains the same, $T_{\perp bf}=T_{\perp bi}=T_{\parallel bi}=T_{bi}$. As a result, the temperature anisotropy ratio after acceleration, $T_{\parallel bf}/T_{\perp bf}=T_{bi}/2e_bV$ (nonrelativistic) or $T_{\parallel bf}/T_{\perp bf}=(T_{bi}/m_bc^2\gamma_b^2)$ (relativistic), can become very small. This reduction in longitudinal temperature provides the free energy to drive collective temperature anisotropy instabilities. Such instabilities may lead to a deterioration of the beam quality (emittance growth, halo particle production, etc.). These instabilities may also lead to an increase in the longitudinal velocity spread, which will make focusing the beam difficult, and may impose a limit on the beam luminosity and the minimum spot size achievable in focusing experiments.

There is a significant amount of literature dedicated to the study of collective instabilities due to temperature anisotropy in intense charged particle beams. The electrostatic Harris instability has been studied theoretically for beams with a Kapchinskij-Vladimirskij (KV) distribution,[16,17] and for a two-temperature Maxwellian distribution,[8,9] and also computationally using particle-in-cell simulations.[18–22] The early numerical studies of this instability used the electrostatic particle-in-cell (PIC) code WARP, which is sufficiently noisy that resolving the linear stage of the instability with sufficient accuracy is difficult. Our previous numerical studies of the Harris instability used the eigenmode code bEASt,[5,6] and the δf particle-in-cell code BEST,[8,9,11] and allowed us to investigate both the linear and nonlinear stages of the Harris instability in considerable detail. The eigenmode code bEASt has also been used to study the linear stage of the electromagnetic Weibel instability.[7]

[a)]Paper WI1 3, Bull. Am. Phys. Soc. **51**, 333 (2006).
[b)]Invited speaker.

This paper reviews recent advances in the theory and simulation of collective instabilities in intense charged particle beams caused by large temperature anisotropy. We also describe new simulation tools that have been developed to study these instabilities. Results of the investigations that identify the instability growth rates, levels of saturations, and conditions for quiescent beam propagation are also discussed.

The organization of this paper is the following. In Sec. II and III, we discuss the physical mechanism for the electrostatic Harris and electromagnetic Weibel instabilities in intense charged particle beams with large temperature anisotropy. The beam eigenmode and spectra (bEASt) code[5–7] developed to study linear properties of these instabilities is described in Sec. IV. The nonlinear δf beam equilibrium, stability, and transport (BEST) code[8–13] has recently been updated to include the electromagnetic Darwin model,[23] and is briefly described in Sec. V. In Sec. VI, we summarize several important simulation results obtained using the linear code bEASt and the nonlinear δf code BEST. Finally, conclusions are summarized in Sec. VII.

II. THE ELECTROSTATIC HARRIS INSTABILITY

For simplicity, the subsequent analysis is carried out in the beam frame ($V_b=0$). The laboratory frame expressions for frequencies and growth rates and their dependence on wave number can be readily obtained by applying the Lorentz transformation to the frequencies and wave numbers in the beam frame.[24] In what follows, it is convenient to introduce the effective *depressed* betatron frequency $\omega_{\beta\perp}$ defined by[9]

$$\omega_{\beta\perp}^2 = \frac{2T_{\perp b}}{m_b r_b^2} = \omega_f^2 - \bar{\omega}_{pb}^2/2, \tag{1}$$

where $T_{\perp b}$ is the transverse beam temperature, r_b is the root-mean-square beam radius, e_b and m_b are the charge and mass of a beam particle, and

$$\bar{\omega}_{pb}^2 = \frac{4\pi e_b^2}{m_b r_b^2}\int_0^{r_w} dr r n_b(r) \tag{2}$$

is the average beam plasma frequency-squared, where $n_b(r)$ is the radial density profile of the beam particles and r_w is the radius of the perfectly conducting wall. The normalized tune depression $\bar{\nu}/\nu_0$ is defined by

$$\frac{\bar{\nu}}{\nu_0} \equiv \frac{\omega_{\beta\perp}}{\omega_f}, \tag{3}$$

where ω_f=const is the transverse frequency associated with the applied focusing field in the smooth-focusing approximation.

We now briefly illustrate the physical mechanism for the electrostatic Harris instability in intense particle beams. As shown in previous studies,[5,6,8,9,11] the dipole mode has the highest growth rate, and for $T_{\parallel b}=0$ the growth rate is an increasing function of $k_z r_b$ and approaches a maximum value for $k_z^2 r_b^2 \gg 1$. Therefore, we consider dipole-mode perturbations with $k_z^2 r_b^2 \gg 1$, which in lowest order correspond to a displacement of the beam charge mainly along the beam propagation direction, arranged as a dipole-mode perturbation as shown in Fig. 1. One can distinguish three possibilities: $\bar{\omega}_{pb} \gg \omega_{\beta\perp}$, $\bar{\omega}_{pb} \ll \omega_{\beta\perp}$, and $\bar{\omega}_{pb} \approx \omega_{\beta\perp}$. If $\bar{\omega}_{pb} \gg \omega_{\beta\perp}$, the charge oscillation will be mostly along the beam propagation direction due to the electrostatic restoring force, and as a result, the mode frequency will be close to the plasma frequency $\omega \approx \bar{\omega}_{pb}$. In the opposite limit, when $\bar{\omega}_{pb} \ll \omega_{\beta\perp}$, the charge perturbations will oscillate with the frequency $\omega_{\beta\perp}$, mainly in the direction transverse to the beam propagation direction due to the restoring betatron force. In this case, the mode frequency will be close to the average betatron frequency $\omega_{\beta\perp}$. Finally, if $\bar{\omega}_{pb} \approx \omega_{\beta\perp}$, the charge perturbation, moved longitudinally by the electrostatic restoring force, will at the same time traverse the beam transversely. In this case, the arrangement of the charge perturbation does not change, and the mode will have approximately zero frequency with Re $\omega=0$. If one now examines the motion of an individual particle in this unchanging dipole electric field $E_z \sim x_\perp$, with longitudinal acceleration $d^2z/dt^2 \sim E_z \sim x_\perp \sim \cos(\omega_{\beta\perp} t)$, one finds that during one-half period of oscillation each particle will acquire a longitudinal displacement Δz that is opposite to the direction of the electric field at this point in space. This means that the particle will move toward the excess charge, and therefore the charge perturbation will be enhanced, which will result in instability with Im $\omega > 0$. One can also see the effects that longitudinal temperature has on the instability. If, during one-half period of transverse oscillation $\pi/\omega_{\beta\perp}$, a particle with average speed $v_{\parallel b}^{\text{th}}$ travels a distance larger than the half-wavelength of the perturbation $\lambda_z/2$, then the perturbation enhancement shown in Fig. 1 will not occur, and the instability is absent. This provides the threshold condition for the onset of instability, i.e.,

$$\lambda_z \gtrsim v_{\parallel b}^{\text{th}} \frac{2\pi}{\omega_{\beta\perp}} \Rightarrow \frac{T_{\parallel b}}{T_{\perp b}} \lesssim \frac{2}{k_z^2 r_b^2}, \tag{4}$$

where use has been made of Eq. (1). Since we have assumed $k_z^2 r_b^2 \gg 1$, Eq. (4) implies that the threshold for instability satisfies $T_{\parallel b}/T_{\perp b} \ll 1$. We can now summarize the necessary

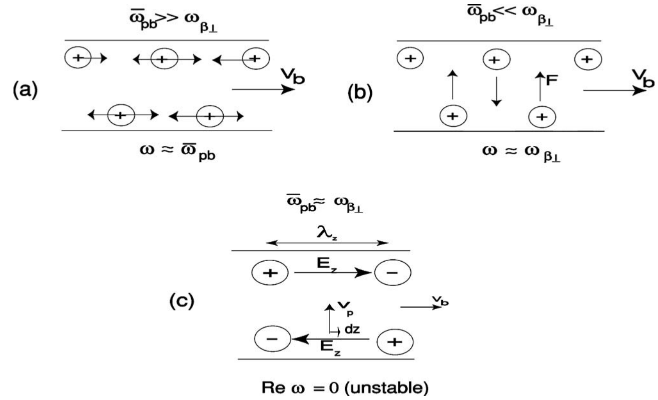

FIG. 1. Physical mechanism for the electrostatic Harris instability in intense particle beams for the case of a dipole-mode perturbation. Three possibilities are illustrated: (a) for $\bar{\omega}_{pb} \gg \omega_{\beta\perp}$, the mode frequency is $\omega \approx \bar{\omega}_{pb}$; (b) for $\bar{\omega}_{pb} \ll \omega_{\beta\perp}$, the mode frequency is $\omega \approx \omega_{\beta\perp}$; and (c) for $\bar{\omega}_{pb} \approx \omega_{\beta\perp}$, the mode is purely growing with Re $\omega=0$ and Im $\omega \sim \omega_{\beta\perp}$.

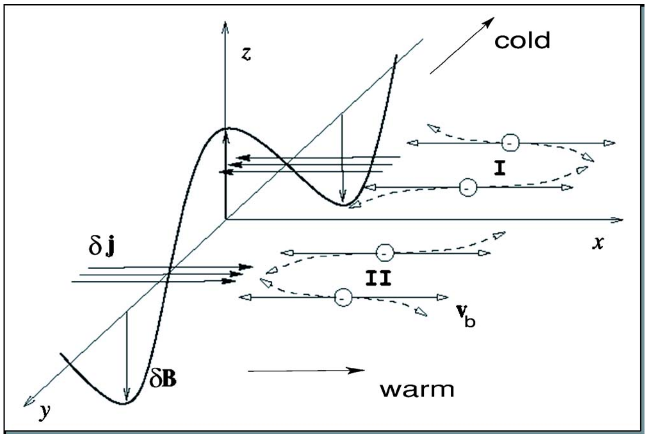

FIG. 2. Mechanism for Weibel instability.

conditions for instability as follows. The instability exists for sufficiently intense beams ($\bar{\omega}_{pb} \approx \omega_{\beta\perp}$) with large temperature anisotropy ($T_{\|b}/T_{\perp b} \ll 1$). Moreover, unstable modes have short wavelengths with $k_z^2 r_b^2 \gg 1$. A more quantitative description of the instability mechanism following the physical picture described above can be found in Refs. 5 and 6.

III. THE ELECTROMAGNETIC WEIBEL INSTABILITY

Another instability known from the study of electrically neutral plasmas that is also driven by temperature anisotropy is the electromagnetic Weibel instability.[15,25–28] The filamentation instability of intense charged particle beams propagating in neutralizing background plasma is a similar instability, and is also often called the Weibel instability. The mechanism for the Weibel instability[7,15] is illustrated in Fig. 2. An initial current perturbation creates a magnetic-field perturbation that in turn acts through the $\mathbf{v}\times\mathbf{B}/c$ force on particles moving with characteristic thermal velocity to displace them in the direction shown in Fig. 2, which enhances the initial current perturbation. This results in a purely growing perturbation with real frequency Re $\omega=0$. Since the driving force is magnetic, the instability is weak, with growth rate proportional to $v_{\rm th}/c$. For the case of a one-component beam, the finite transverse geometry of the beam makes a detailed analytical description difficult. We provide here a simple physical model based mainly on the results of simulations, which will be presented later.

We consider a charged particle beam confined inside a circular conducting pipe of radius r_w by an external linear force $\mathbf{F}=-m_b\omega_f^2\mathbf{x}_\perp$ in the smooth-focusing approximation. For simplicity, the analysis is carried out in the beam frame ($V_b=0$). The beam is confined in the transverse direction provided $\hat{\omega}_{pb}^2/2\omega_f^2<1$. Here, $\hat{\omega}_{pb}^2=4\pi e_b^2\hat{n}_b/m_b$ is the on-axis ($r=0$) plasma frequency-squared, and ω_f is the average oscillation frequency of a beam particle with mass m_b and charge e_b in the applied focusing field. It follows from the numerical studies presented later in this paper that the fastest growing modes correspond to rigid rotations of the beams slices with $\delta J_\theta \sim r$ for $\hat{\omega}_{pb}^2/2\omega_f^2 \to 1$. The growth rate is an increasing function of $k_z r_b$ and approaches a maximum value for $k_z^2 r_b^2 \gg 1$. Therefore, in leading order, the perturbed magnetic field is given approximately by $\delta\mathbf{B}\simeq ik_z\delta A_\theta\mathbf{e}_r$ for $k_z^2 r_b^2 \gg 1$. From Maxwell's equations it follows that

$$\delta A_\theta(\mathbf{x},t)=\hat{A}_\theta\frac{r}{r_b}\exp[i(k_z z-\omega t)]. \tag{5}$$

The longitudinal equation of motion for a beam particle becomes

$$\ddot{z}=-\frac{e_b}{m_b}\frac{v_\theta}{c}\delta B_r=-ik_z\frac{e_b}{m_b}\hat{A}_\theta\frac{r(t)v_\theta(t)}{cr_b}\exp[i(k_z z_0-\omega t)]. \tag{6}$$

In the smooth-focusing approximation, the unperturbed motion is in a cylindrically symmetric potential $U(r)$, and therefore the angular momentum is conserved, i.e., $r(t)v_\theta(t)=const.$ Integrating Eq. (6) with respect to time t, we obtain

$$z(t)=i\frac{k_z}{\omega^2}\frac{e_b}{m_b}\hat{A}_\theta\frac{r(t)v_\theta(t)}{cr_b}\exp[i(k_z z_0-\omega t)]=\frac{v_\theta}{\omega^2}\frac{e_b\delta B_r}{m_b c}. \tag{7}$$

The average axial displacement is given by $\langle z\rangle\sim\langle v_\theta\rangle=0$, and therefore the density perturbation $\delta n_b=-\bar{n}_b\partial\langle z\rangle/\partial z$ is zero. Therefore, for the current perturbation, we obtain

$$\frac{\partial\delta J_\theta}{\partial t}+\frac{\partial}{\partial z}\left(e_b\bar{n}_b\frac{\partial\langle v_\theta z\rangle}{\partial t}\right)=0,$$
$$\delta J_\theta=-e_b\bar{n}_b\frac{\partial\langle v_\theta z\rangle}{\partial z}=-\frac{e_b^2\bar{n}_b}{m_b c}\frac{\langle v_\theta^2\rangle}{\omega^2}\frac{\partial\delta B_r}{\partial z}. \tag{8}$$

Substituting Eq. (8) into Maxwell's equation $\partial\delta B_r/\partial z=4\pi\delta J_\theta/c$, we obtain the simple dispersion relation

$$1=-\frac{\bar{\omega}_{pb}^2}{\omega^2}\frac{\langle v_\theta^2\rangle}{c^2}, \tag{9}$$

where $\bar{\omega}_{pb}^2=4\pi e_b^2\bar{n}_b/m_b$ is the average beam plasma frequency squared. Noting that $T_{\perp b}=m_b\langle v_\theta^2+v_r^2\rangle/2=m_b\langle v_\theta^2\rangle$, we can express the growth rate in this simple model of the Weibel instability as

$$\gamma=\bar{\omega}_{pb}\sqrt{\frac{T_{\perp b}}{m_b c^2}}=\frac{\bar{\omega}_{pb}}{\sqrt{2}}\frac{v_{\perp b}^{\rm th}}{c}\approx 0.71\bar{\omega}_{pb}\frac{v_{\perp b}^{\rm th}}{c}, \tag{10}$$

where $v_{\perp b}^{\rm th}=\sqrt{2T_{\perp b}/m_b}$ is the transverse thermal velocity.

IV. DESCRIPTION OF BEAM EIGENMODE AND SPECTRA (BEAST) CODE

For an arbitrary equilibrium distribution, one cannot solve the stability problem analytically and must employ numerical techniques. To investigate stability properties numerically, we make use of the linear eigenmode method, which searches for the roots of the matrix dispersion relation, as implemented in the beam eigenmode and spectra (bEASt) code.[5–7]

The bEASt code assumes small-amplitude electrostatic perturbations of the form

$$\delta\phi(\mathbf{x},t) = \hat{\delta\phi}(r)\exp(im\theta + ik_z z - i\omega t), \quad (11)$$

where $\delta\phi(\mathbf{x},t)$ is the perturbed electrostatic potential, k_z is the axial wave number, m is the azimuthal mode number, and ω is the complex oscillation frequency, with Im $\omega>0$ corresponding to instability (temporal growth). We also assume that the beam is located inside a perfectly conducting cylindrical pipe with radius r_w. Electromagnetic perturbations are assumed to be of the form

$$\delta A_\theta(\mathbf{x},t) = \hat{\delta A}(r)\exp[i(k_z z - \omega t)]. \quad (12)$$

All perturbations are about the thermal equilibrium distribution with temperature anisotropy $(T_{\perp b} > T_{\parallel b})$ described *in the beam frame* ($V_b=0$ and $\gamma_b=1$) by the self-consistent axisymmetric Vlasov equilibrium

$$f_b^0(r,\mathbf{p}) = \frac{\hat{n}_b}{(2\pi m_b)^{3/2}T_{\perp b}T_{\parallel b}^{1/2}}\exp\left(-\frac{H_\perp}{T_{\perp b}} - \frac{p_z^2}{2m_b T_{\parallel b}}\right). \quad (13)$$

Here, $H_\perp = p_\perp^2/2m_b + (1/2)m_b\omega_f^2(x^2+y^2) + e_b\phi^0(r)$ is the single-particle Hamiltonian for transverse particle motion, and ω_f=const is the transverse focusing frequency.

The electrostatic perturbation amplitude is expressed as $\hat{\delta\phi}(r) = \Sigma_n \alpha_n \phi_n(r)$, where $\{\alpha_n\}$ are constants, and the complete set of vacuum eigenfunctions $\{\phi_n(r)\}$ is defined by $\phi_n(r) = A_n J_m(\lambda_n^m r/r_w)$. Here, λ_n^m is the nth zero of $J_m(\lambda_n^m)=0$, and $A_n = \sqrt{2}/[r_w J_{m+1}(\lambda_n)]$ is a normalization constant such that $\int_0^{r_w} dr r\phi_n(r)\phi_{n'}(r) = \delta_{n,n'}$. Electromagnetic perturbations are also expanded in terms of the complete set of vacuum eigenfunctions $\hat{\delta A}(r) = \Sigma_n \alpha_n A_n(r)$, where $A_n(r) = A_n J_1(\lambda_n^1 r/r_w)$ and $J_1(\lambda_n^1)=0$. Using the method of characteristics, analysis of the linearized Vlasov-Maxwell equations leads to an infinite-dimension matrix dispersion equation,[5–9,11,15]

$$\sum \alpha_n D_{n,m}(\omega) = 0, \quad (14)$$

where the elements of the dispersion matrix $D_{n,n'}(\omega)$ are defined by

$$D_{n,n'}^{\mathrm{el}}(\omega) = \frac{J_{m+1}^2(\lambda_n^m)}{2}(\lambda_n^{m^2} + k_z^2 r_w^2)\delta_{n,n'} + \chi_{n,n'}^{\mathrm{el}}(\omega) \quad (15)$$

for electrostatic perturbations, and by

$$D_{n,n'}^{\mathrm{em}}(\omega) = \frac{J_2^2(\lambda_n^1)}{2}\left(\lambda_n^{1^2} + k_z^2 r_w^2 - r_w^2\frac{\omega^2}{c^2}\right)\delta_{n,n'} + \chi_{n,n'}^{\mathrm{em}}(\omega) \quad (16)$$

for electromagnetic perturbations. Here, $\chi_{n,n'}$ is the beam-induced susceptibility and is defined by

$$\chi_{n,n'}^{\mathrm{el}}(\omega) = \frac{r_w^2}{\lambda_d^2}q_{n,n'} + \int_0^\infty ds\,\exp\left(is\omega - \frac{s^2k_z^2T_\parallel}{2m_b}\right) \times\left[i\omega + \left(1 - \frac{T_\parallel}{T_\perp}\right)\frac{sk_z^2T_\perp}{2m_b}\right]Q_{n,n'}^{\mathrm{el}}(s) \quad (17)$$

for electrostatic perturbations,[5,6,8,9,11] where

$$Q_{n,n'}^{\mathrm{el}}(s) = \frac{1}{m_b\lambda_d^2}\sum_p \int \frac{dP_\theta}{\omega_r}\frac{dH_\perp}{T_{\perp b}}\exp\left[-\frac{H_\perp}{T_{\perp b}}\right] \times (I_n^{p,m})^* I_{n'}^{p,m}\exp[-is(p\omega_r + m\omega_\theta)]. \quad (18)$$

In Eqs. (17) and (18), $q_{n,n'}$ and $I_n^{p,m}$ are defined by

$$q_{n,n'} = \int_0^1 dx x N(x) J_m(\lambda_n^m x) J_m(\lambda_{n'}^m x), \quad (19)$$

and the orbit integral $I_n^{p,m}$ is defined by

$$I_n^{p,m}(H_\perp,P_\theta) = \int_0^{T_r}\frac{d\tau}{T_r}J_m\left[\frac{\lambda_n r(\tau)}{r_w}\right] \times\exp\{-ip\omega_r\tau + im[\theta(\tau) - \omega_\theta\tau]\}. \quad (20)$$

The beam-induced susceptibility for low-frequency electromagnetic modes with $\omega \ll \omega_f$ is defined by[7,15]

$$\chi_{n,n'}^{\mathrm{em}}(\omega) = \frac{\hat{\omega}_{pb}^2}{c^2}\left\{1 - \frac{T_\parallel}{T_\perp}\left[1 + \frac{\omega}{k_z v_\parallel^{\mathrm{th}}}Z\left(\frac{\omega}{k_z v_\parallel^{\mathrm{th}}}\right)\right]\right\}Q_{n,n'}^{\mathrm{em}}, \quad (21)$$

where

$$Q_{n,n'}^{\mathrm{em}} = \int \frac{dP_\theta P_\theta^2}{m_b^2\omega_r}\frac{dH_\perp}{T_{\perp b}^2}\exp\left[-\frac{H_\perp}{T_{\perp b}}\right](I_n)^* I_{n'}. \quad (22)$$

The orbit integral I_n is defined by

$$I_n(H_\perp,P_\theta) = \int_0^{T_r}\frac{d\tau}{T_r}J_1\left[\frac{\lambda_n^1 r(\tau)}{r(\tau)}\right]. \quad (23)$$

Here, P_θ is the canonical angular momentum, $\hat{\omega}_{pb}^2 = 4\pi e_b^2\hat{n}_b/m_b$ is the on-axis plasma frequency-squared, $\lambda_d^2 = T_{\perp b}/4\pi e_b^2\hat{n}_b$ is the perpendicular Debye length-squared, and $v_{\parallel b}^{\mathrm{th}} = \sqrt{2T_{\parallel b}/m_b}$. In the orbit integrals in Eqs. (20) and (23), $r(\tau)$ and $\theta(\tau)$ are the transverse orbits in the equilibrium field configuration such that $\theta(0)=0$, $r(0)=r_{\min}(H_\perp,P_\theta)$ is the minimum radial excursion of the particle trajectory undergoing periodic motion with frequency $\omega_r(H_\perp,P_\theta) = 2\pi/T_r$, and $\omega_\theta(H_\perp,P_\theta) = \theta(T_r)/T_r$ is the average frequency of angular rotation. In Eq. (18), $(\,)^*$ denotes complex conjugate, and $N(x) = n_b^0(xr_w)/\hat{n}_b$ is the normalized density profile, where $n_b^0(r) = \int d^3p f_b^0(r,\mathbf{p})$.

The beam eigenmode and spectra (bEASt) code solves Eq. (14) in several steps. First, the particle orbits $r(\tau)$ and $\theta(\tau)$ in the equilibrium field configuration are calculated for one complete oscillation period T_r, and the frequencies $\omega_r(H_\perp,P_\theta)$ and $\omega_\theta(H_\perp,P_\theta)$ are obtained. Next, a fast Fourier transform (FFT) is used to calculate the orbit integrals in Eqs. (20) and (23). Then, in the next step, the matrices $Q_{n,n'}(s)$ [Eqs. (18) and (22)] and $q_{n,n'}$ [Eq. (19)] are calculated, stored, and then used repeatedly to recalculate the beam-induced susceptibility [Eqs. (17) and (21)] and dispersion matrix [Eqs. (15) and (16)] during the search for the eigenvector of the dispersion matrix $D_{n,n'}(\omega)$ [Eq. (14)] with zero eigenvalue. Note that the matrices $Q_{n,n'}(s)$ and $q_{n,n'}$ are calculated only once, thanks to the separation of the particle variables $(H_\perp,P_\theta,r,\theta)$ from the dispersion equation variables ω and k_z in Eq. (17). The typical number of particle trajectories used in the calculations is 300, with 16 time steps during one oscillation period T_r, which is significantly less than the number of particles and time steps used in PIC simulations.[8,9,11] The method described here works well for finding the unstable modes, or slightly damped modes. For highly damped modes, an accurate integration in Eq. (17) requires calculation of the matrix $Q^{\rm el}_{n,n'}(s)$ for values of $s > |\mathrm{Im}\,\omega|/(k_z^2 T_\perp/m_b)$, which can be demanding computationally.

V. DESCRIPTION OF BEAM EQUILIBRIUM, STABILITY, AND TRANSPORT (BEST) CODE

To investigate the nonlinear stage of instability, we make use of the nonlinear δf method[29] described below, as implemented in the beam equilibrium, stability, and transport (BEST) code.[1,10,13] This code has recently been extended to include electromagnetic Darwin model equations, as we now describe. The Darwin model has a long history. It was originally proposed by Darwin to study relativistic corrections to atomic energy levels. He found a particle Lagrangian that described the electromagnetic interaction of charged particles accurate up to second order in v/c, where v is the particle velocity and c is the speed of light. The Lagrangian Darwin model was later reformulated as a model with its own set of field equations and applied to study low-frequency electromagnetic phenomena in electrically neutral plasmas. As it turns out, the original Lagrangian Darwin model is equivalent to neglecting the transverse part of the displacement current in Ampere's law. As a key consequence, high-frequency light waves are eliminated from the Maxwell-Vlasov system. This greatly relaxes the time-step restrictions for numerical simulations, and it avoids the Courant condition $\Delta x/c\Delta t < 1$. The resulting Maxwell equations are elliptic and depend only on instantaneous particle quantities. Also, since high-frequency light waves are eliminated, the simulation noise is greatly reduced. The reduced Maxwell equations for the Darwin model used in the modified BEST code can be expressed as

$$\nabla\cdot\mathbf{E}^L = 4\pi\rho, \tag{24}$$

$$\nabla\times\mathbf{B} = (4\pi/c)\mathbf{J}^T, \tag{25}$$

$$\nabla\times\mathbf{E}^T = -(1/c)\partial\mathbf{B}/\partial t, \tag{26}$$

$$\nabla\cdot\mathbf{B} = 0, \tag{27}$$

where

$$\mathbf{E}^L = -\nabla\phi, \tag{28}$$

$$\mathbf{J}^T = \mathbf{J} - \frac{1}{4\pi}\frac{\partial\nabla\phi}{\partial t}, \tag{29}$$

and

$$\nabla\times\mathbf{E}^L = 0, \quad \nabla\cdot\mathbf{E}^T = 0, \quad \nabla\cdot\mathbf{J}^T = 0. \tag{30}$$

Expressing $\mathbf{B}=\nabla\times\mathbf{A}$, and using the Coulomb gauge with $\nabla\cdot\mathbf{A}=0$, Ampere's equation takes the form

$$\nabla^2\mathbf{A} = -\frac{4\pi}{c}\mathbf{J}^T, \tag{31}$$

where

$$\mathbf{E}^T = -\frac{1}{c}\frac{\partial\mathbf{A}}{\partial t}. \tag{32}$$

For comparison, the original Ampere's law takes the form $\nabla^2\mathbf{A}-(1/c^2)\partial^2\mathbf{A}/\partial t^2 = -4\pi/c\mathbf{J}^T$. However, as noted previously,[30] the presence of the time derivative of the vector potential in the equations of motion $d\mathbf{p}/dt = -(q/c)\partial\mathbf{A}/\partial t + \cdots$ can cause numerical instabilities in particle simulations because of the time-centering problem in particle pushing. These difficulties are avoidable if we introduce the canonical momentum $\mathbf{P}=\mathbf{p}+(q/c)\mathbf{A}$.[30] Specifically, the equations of motion become

$$\frac{d\mathbf{x}}{dt} = \mathbf{v}, \tag{33}$$

$$\frac{d\mathbf{P}}{dt} = \frac{q}{c}\nabla(\mathbf{v}\cdot\mathbf{A}) - q\nabla\phi - m\omega_\beta^2\mathbf{x}_\perp. \tag{34}$$

Here

$$\mathbf{v} = \mathbf{p}/m\gamma, \quad \gamma = [1+(\mathbf{p}/mc)^2]^{1/2}, \quad \mathbf{p} = \mathbf{P} - \frac{q}{c}\mathbf{A}. \tag{35}$$

Thus, by transforming variables from mechanical momentum $\mathbf{p}$ to canonical momentum $\mathbf{P}$, the time derivative of $\mathbf{A}$ conveniently disappears from the equations of motion. To calculate the particle trajectories in Eqs. (33) and (34), one needs to calculate only the electrostatic potential ϕ and the electromagnetic vector potential $\mathbf{A}$. The Vlasov equation in the new variables can be expressed as

$$\frac{dF}{dt} \equiv \frac{\partial F}{\partial t} + \frac{d\mathbf{x}}{dt}\cdot\frac{\partial F}{\partial\mathbf{x}} + \frac{d\mathbf{P}}{dt}\cdot\frac{\partial F}{\partial\mathbf{P}} = 0, \tag{36}$$

where the characteristics are defined by Eqs. (33) and (34). The electrostatic potential ϕ is determined from Poisson's equation

$$\nabla^2\phi = -4\pi\rho, \tag{37}$$

and the electromagnetic vector-potential $\mathbf{A}$ is determined by solving a system of coupled equations of the Helmholtz type, i.e.,

$$\left(\nabla^2 - \frac{\omega_p^2}{c^2}\right)\mathbf{A} + \nabla\psi = -\frac{4\pi}{c}\mathbf{J}_p, \tag{38}$$

$$\nabla\cdot\mathbf{A} = 0. \tag{39}$$

Here the factor $\omega_p^2/c^2 = (4\pi q^2/mc^2)\int d^3P F/\gamma$ arises from introducing the canonical momentum, the potential ψ formally solves $\nabla^2\psi = -(4\pi/c)\nabla\cdot\mathbf{J}$, which removes the longitudinal part of the current, and the current $\mathbf{J}_p$ occurring in Eq. (38) is defined by

$$\mathbf{J}_p = q \int d^3P \frac{\mathbf{P}}{\gamma m} F. \tag{40}$$

For the case of heavy ions with $r_b^2\omega_p^2/c^2 \ll 1$, the skin term can be neglected in Eq. (38), and the above system of equations is linear. For electrons, the skin term is not generally negligible, and the system is nonlinear and is solved by iteration. For a perfectly conducting cylindrical wall of radius r_w, the boundary conditions for ϕ, $\mathbf{A}$, and ψ are especially simple, i.e.,

$$\phi_{r_w} = \mathbf{A}_{r_w} = \psi_{r_w} = 0. \tag{41}$$

The boundary condition for ψ follows from the fact that $\psi = -(1/c)\partial\phi/\partial t$.

In the corresponding δf formalism, the solutions to the nonlinear Vlasov-Maxwell equations are expressed as $F = F_0 + \delta f$, $\phi = \phi_0 + \delta\phi$, $\mathbf{A} = \mathbf{A}_0 + \delta\mathbf{A}$, where $(F_0, \phi_0, \mathbf{A}_0)$ are known equilibrium solutions $(\partial/\partial t = 0)$. The perturbed distribution is determined from

$$\frac{d\delta f}{dt} = -\left.\frac{d\mathbf{x}}{dt}\right|_\delta \cdot \frac{\partial F_0}{\partial \mathbf{x}} - \left.\frac{d\mathbf{P}}{dt}\right|_\delta \cdot \frac{\partial F_0}{\partial \mathbf{P}}, \tag{42}$$

where $|_\delta$ denotes the perturbed particle trajectories obtained by using the perturbed potentials $\delta\phi$ and $\delta\mathbf{A}$. In the particle simulations using the modified BEST code, the perturbed $\delta f(\mathbf{x}, \mathbf{p}, t)$ is given by the weighted Klimontovich representation,

$$\delta f = \sum_{i=1}^{N} w_i \delta(\mathbf{x} - \mathbf{x}_i)\delta(\mathbf{P} - \mathbf{P}_i). \tag{43}$$

Here, N is total number of particles in the simulation. The weight function w, defined by $w = \delta f/F$, evolves according to

$$\frac{dw}{dt} = (1 - w)\frac{1}{F_0}\frac{d\delta f}{dt}. \tag{44}$$

In the modified BEST code, the nonlinear particle simulations are carried out by iteratively advancing the particle motion, including the weights they carry, and updating the fields by solving the perturbed Maxwell's equations with appropriate boundary conditions at the cylindrical, perfectly conducting wall at radius r_w.

The δf approach is fully equivalent to the original nonlinear Vlasov-Maxwell equations, but the noise associated with representation of the background distribution F_0 in conventional particle-in-cell (PIC) simulations is removed. In the δf approach, the simulation particles are used to represent only a small part of the entire distribution $\delta f = F - F_0$, and therefore the statistical error in the simulations is proportional to $\epsilon_{\delta f} \sim \bar{w}/\sqrt{N}$, whereas the error in PIC simulations is proportional to $\epsilon_{\rm PIC} \sim 1/\sqrt{N}$. Therefore, the typical gain in accuracy in δf simulations compared to PIC simulations with the same number of particles is $\epsilon_{\delta f}/\epsilon_{\rm PIC} = \bar{w}$.[10] This fact allows much more accurate simulations of the nonlinear dynamics and instability thresholds when $|\bar{w}| \ll 1$. In addition, the δf method can be used to study linear stability properties, provided all nonlinear terms in the dynamical equations of motion are neglected. This corresponds to replacing the term

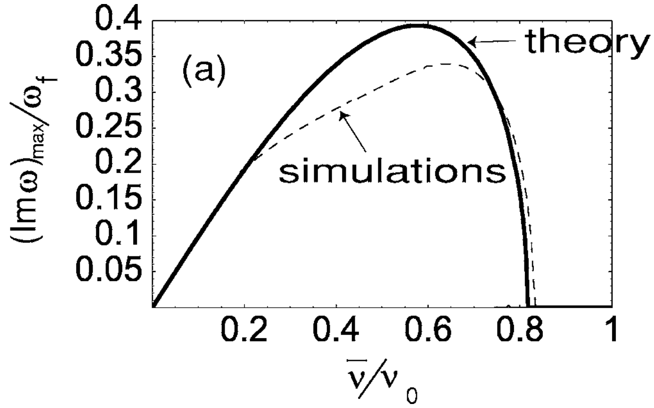

FIG. 3. Plots of the normalized growth rate $(\mathrm{Im}\,\omega)_{\max}/\omega_f$ at maximum growth versus normalized tune depression $\bar{\nu}/\nu_0$ for $T_{\|b}/T_{\perp b} = 0$ and azimuthal mode number $m = 1$ (dotted curve). Results are obtained using the eigenmode code bEASt (Refs. 5 and 6). The thick solid curve corresponds to the simple theoretical estimate from Ref. 6.

$1 - w$ with 1 in Eq. (44) for the weights, and moving the particles along the trajectories calculated in the unperturbed fields ϕ_0 and $\mathbf{A}_0$.

The δf method described above has been implemented in the three-dimensional electromagnetic particle-in-cell code (BEST) in cylindrical geometry with a perfectly conducting cylindrical wall at radius r_w. Maxwell's equations (37)–(39) are solved using fast Fourier transform (FFT) techniques in the longitudinal and azimuthal directions. The particle positions [Eqs. (33) and (34)] and weights [Eq. (44)] are advanced using a second-order predictor-corrector algorithm. The BEST code is parallelized using the message passing interface (MPI) with domain decomposition in the direction of beam propagation. The NetCDF data format is used for large-scale diagnostics and visualization. Typical simulation runs consist of 10^7 simulation particles and are performed on the IBM SP/RS 6000 at NERSC.

VI. NUMERICAL SIMULATIONS OF THE HARRIS AND WEIBEL INSTABILITIES

Detailed simulations of the electrostatic Harris instability using the eignemode code bEASt and the nonlinear δf code BEST have been performed, and results can be found in Refs. 5, 6, 8, 9, and 11. Here, for completeness, we summarize some of the most important results.

Figure 3 shows plots of the normalized growth rate $(\mathrm{Im}\,\omega)_{\max}/\omega_f$ at maximum growth versus normalized tune depression $\bar{\nu}/\nu_0$ for $T_{\|b}/T_{\perp b} = 0$ and azimuthal mode number $m = 1$ (dotted curve). Here wall radius $r_w = 3r_b$. The results are obtained using the eigenmode code bEASt.[5,6] The thick solid curve corresponds to the simple estimate obtained in Ref. 6. Only the $m = 1$ results are shown since it has the largest growth rate. The $m = 1$ dipole mode is purely growing with $\mathrm{Re}\,\omega = 0$ and $(\mathrm{Im}\,\omega)_{\max}/\omega_f \simeq 0.34$ for $\bar{\nu}/\nu_0 \simeq 0.62$. Here, ω_f is the betatron frequency due to the applied focusing field. Note that the instability is absent for $\bar{\nu}/\nu_0 > 0.82$. Therefore, the Harris instability is absent for beams with sufficiently small tune shift $\delta\nu/\nu_0 = (\bar{\nu} - \nu_0)/\nu_0$. Figure 4 shows the threshold value of the anisotropy $T_{\|b}/T_{\perp b}$ as a function of the normal-

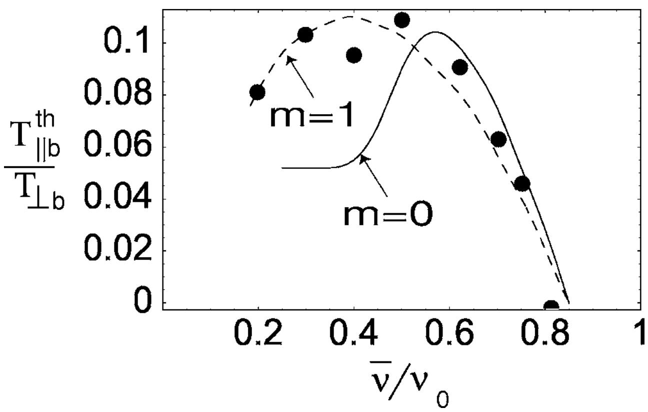

FIG. 4. The longitudinal threshold temperature $T_{\parallel b}^{\mathrm{th}}$ for the onset of the Harris instability normalized to the transverse temperature $T_{\perp b}$ is plotted versus normalized tune depression $\bar{\nu}/\nu_0$ for two values of the azimuthal mode number, $m=0$ (solid line) and $m=1$ (dotted line). The large dots correspond to the longitudinal beam temperature $T_{\parallel b}\equiv m_b\langle v_\parallel^2\rangle$ obtained with the nonlinear δf BEST code after the instability saturates.

ized tune depression $\bar{\nu}/\nu_0$ obtained using the eigenmode code bEASt.[5,6] Note from Fig. 4 that the maximum threshold value, $T_{\parallel b}^{\mathrm{th}}/T_{\perp b}=0.11$, is achieved for moderately intense beams with $\bar{\nu}/\nu_0=0.4$. The curves in Fig. 4 are results obtained with the bEASt code, and the dots correspond to the longitudinal beam temperature $T_{\parallel b}\equiv m_b\langle v_\parallel^2\rangle$ obtained with the nonlinear δf code BEST after the instability saturates. As shown in Refs. 5 and 6, the Harris instability saturates nonlinearly by particle trapping and quasilinear relaxation.

We now present typical numerical results for the Weibel instability obtained using the eigenmode code bEASt, and the linearized version of the δf code BEST, for the case in which $r_w=3r_b$, $T_{\parallel b}/T_{\perp b}=0$, $\partial/\partial\theta=0$. Figure 5 shows plots of the normalized growth rate $(\mathrm{Im}\,\omega)/(\hat{\omega}_{pb}v_{\perp b}^{\mathrm{th}}/c)$ versus k_zr_b obtained for normalized skin depth $c/r_b\hat{\omega}_{pb}=100$ and several values of the normalized depressed tune $\bar{\nu}/\nu_0=0.09(4), 0.4(3), 0.72(2)$. Also shown are the results of a linear simulation using the Darwin BEST code for $\bar{\nu}/\nu_0=0.88, 0.92, 0.95, 0.97(1)$, $c/r_b\hat{\omega}_{pb}=10$, and $T_{\parallel b}/T_{\perp b}=10^{-4}$.

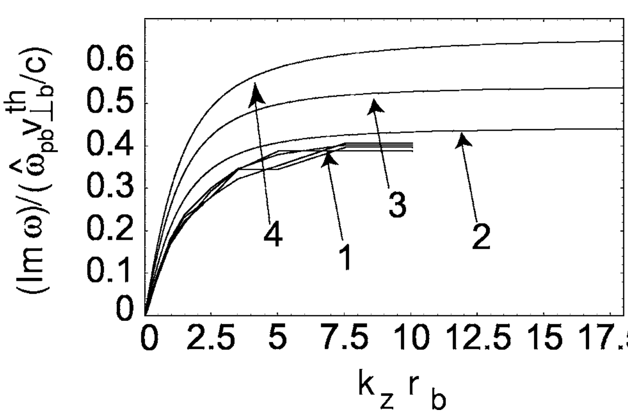

FIG. 5. The normalized growth rate $(\mathrm{Im}\,\omega)/(\hat{\omega}_{pb}v_{\perp b}^{\mathrm{th}}/c)$ of the Weibel instability is plotted versus k_zr_b for normalized skin depth $c/r_b\hat{\omega}_{pb}=100$ and several values of the normalized depressed tune $\bar{\nu}/\nu_0=0.09(4), 0.4(3), 0.72(2)$. Also shown are the results of linear runs using the Darwin BEST code for $\bar{\nu}/\nu_0=0.88, 0.92, 0.95, 0.97(1)$, $c/r_b\hat{\omega}_{pb}=10$, and $T_{\parallel b}/T_{\perp b}=10^{-4}$.

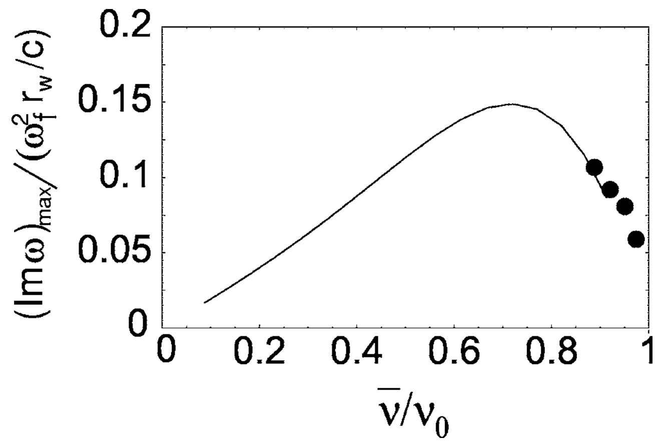

FIG. 6. Plot of the normalized maximum growth rate $(\mathrm{Im}\,\omega)_{\max}/(\omega_f^2r_w/c)$ of the Weibel instability versus the average depressed tune $\bar{\nu}/\nu_0$ for $T_{\parallel b}/T_{\perp b}=0$.

Numerical studies using the eigenmode code bEASt have shown[7] that the results are insensitive to the normalized skin depth provided $c/r_b\hat{\omega}_{pb}\gg 1$. As evident from Fig. 5, the results obtained with the δf code BEST are consistent with the results obtained using the eigenmode code bEASt. Plots of the normalized maximum growth rate $(\mathrm{Im}\omega)_{\max}/(\omega_f^2r_w/c)$ versus the average depressed tune $\bar{\nu}/\nu_0$ for $T_{\parallel b}/T_{\perp b}=0$ and $c/r_b\hat{\omega}_{pb}=100$ obtained using the bEASt code are shown in Fig. 6. The maximum growth rate is achieved for moderately intense beams with $\bar{\nu}/\nu_0\approx 0.73$. The dots are results of linear runs using the Darwin BEST code for $T_{\parallel b}/T_{\perp b}=10^{-4}$ and $c/r_b\hat{\omega}_{pb}=10$. Again, the results obtained using both codes are in good agreement. Figure 7 shows the normalized longitudinal threshold temperature $(T_{\parallel b}^{\mathrm{th}}/T_{\perp b})c^2/r_b^2\hat{\omega}_{pb}^2$ for the onset of instability plotted versus the normalized tune depression $\bar{\nu}/\nu_0$ for normalized skin depth $c/r_b\hat{\omega}_{pb}=100$.

The nonlinear stage of the Weibel instability is illustrated in Figs. 8–11 for a beam with $\bar{\nu}/\nu_0=0.88$ and initial temperature ratio $T_{\parallel b}/T_{\perp b}=10^{-4}$ and $c/r_b\hat{\omega}_{pb}=10$. Figure 8 shows a plot of the effective longitudinal temperature $T_{\parallel b}\equiv m_b\langle v_\parallel^2\rangle$ normalized to the initial longitudinal temperature $T_{\parallel b}^0$ as a function of time. The initial linear stage is followed by a stage where the temperature grows superexponentially due to particle trapping. At later stages, the temperature varies

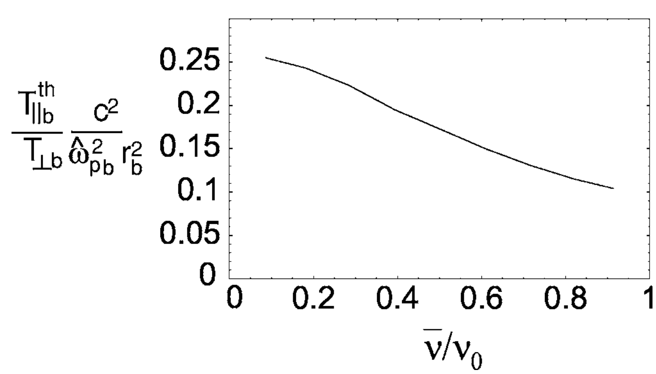

FIG. 7. The normalized longitudinal threshold temperature $(T_{\parallel b}^{\mathrm{th}}/T_{\perp b})c^2/r_b^2\hat{\omega}_{pb}^2$ for the onset of the Weibel instability is plotted versus the normalized tune depression $\bar{\nu}/\nu_0$ for normalized skin depth $c/r_b\hat{\omega}_{pb}=100$.

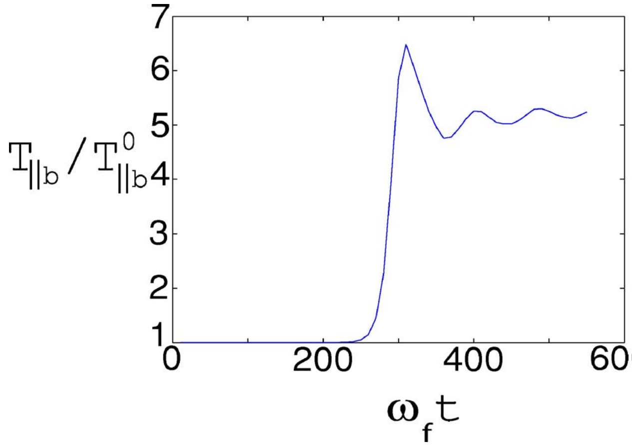

FIG. 8. Plot of the effective longitudinal temperature $T_{\parallel b} \equiv m_b \langle v_\parallel^2 \rangle$ normalized to the initial longitudinal temperature $T_{\parallel b}^0$ as a function of time for a beam with $\bar{\nu}/\nu_0 = 0.88$ and initial temperature ratio $T_{\parallel b}/T_{\perp b} = 10^{-4}$ and $c/r_b \hat{\omega}_{pb} = 10$.

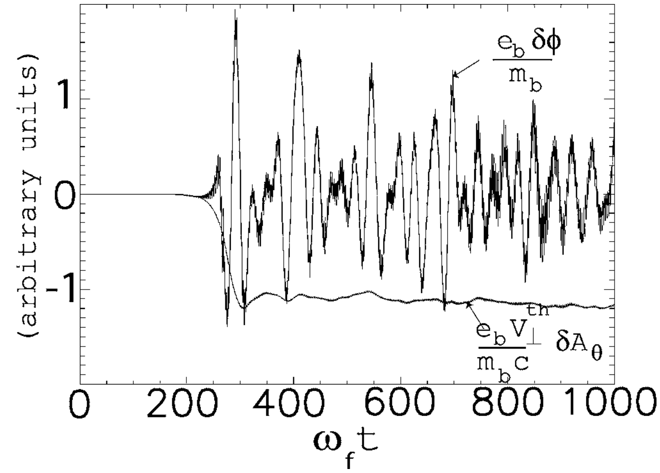

FIG. 10. Time history of the electrostatic potential $e_b \delta\phi / m_b$ and azimuthal component of the vector potential $e_b v_\perp^{\text{th}} \delta A_\theta / m_b c$ are plotted versus time for a beam with $\bar{\nu}/\nu_0 = 0.88$ and initial temperature ratio $T_{\parallel b}/T_{\perp b} = 10^{-4}$ and $c/r_b \hat{\omega}_{pb} = 10$.

slightly due to quasilinear mixing. Figure 9 shows plots of the z-averaged longitudinal velocity distribution at $t=0$, and at a time after saturation. After saturation, the longitudinal velocity distribution remains nearly Maxwellian. Figure 10 shows the time history of the electrostatic potential $e_b \delta\phi / m_b$ and the azimuthal component of the vector potential $e_b v_\perp^{\text{th}} \delta A_\theta / m_b c$. At saturation, both have similar normalized amplitudes, and the particles become trapped both electrostatically and electromagnetically. This is a particular feature of the Weibel instability in intense non-neutral beams. Figure 11 shows the normalized parallel velocity $v_\parallel / v_{\parallel b}^{\text{th}}$ of an individual test particle as a function of time. One can see clearly that the particle motion becomes trapped when the instability saturates.

VII. CONCLUSIONS

To summarize, we have generalized the analysis of the classical Harris and Weibel instabilities to the case of a one-component intense charged particle beam with anisotropic temperature. For a long, coasting beam, the delta-f particle-in-cell code BEST and the eigenmode code bEASt have been used to determine the detailed 3D stability properties over a wide range of temperature anisotropy and beam intensity. It has been shown that intense beams with $\bar{\nu}/\nu_0 < 0.82$ and $T_{\parallel b}/T_{\perp b} < 0.11$ are linearly unstable to electrostatic perturbations (Harris-type instability). The instability is kinetic in nature and is due to the coupling of the particles' transverse betatron motion with the longitudinal plasma oscillations excited by the perturbation. It has also been shown that finite transverse geometry introduces the Weibel instability threshold $T_{\parallel b}^{\text{th}}/T_{\perp b} \approx 10^{-0.7} r_b^2 \hat{\omega}_{pb}^2 / c^2 \sim (v_{\perp b}^{\text{th}}/c)^2$. This makes the Weibel instability much less dangerous for intense beams with normalized tune $\bar{\nu}/\nu_0 < 0.82$. This is because such intense beams are unstable due to the electrostatic Harris instability, which saturates at much larger longitudinal temperature, $(T_{\parallel b}^{\text{th}}/T_{\perp b})^{\text{Weibel}} \ll (T_{\parallel b}^{\text{th}}/T_{\perp b})^{\text{Harris}} \approx 0.1$, and has

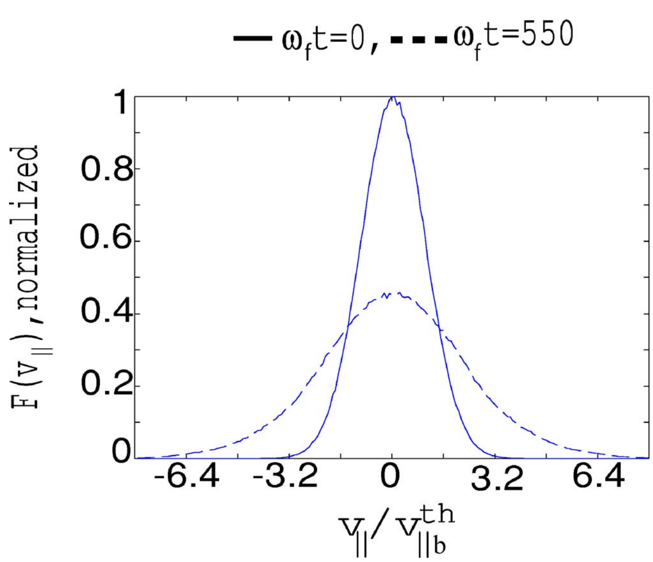

FIG. 9. Plots of z-averaged longitudinal velocity distribution. The dashed curve is for $\omega_f t = 550$ and the solid curve is for $\omega_f t = 0$.

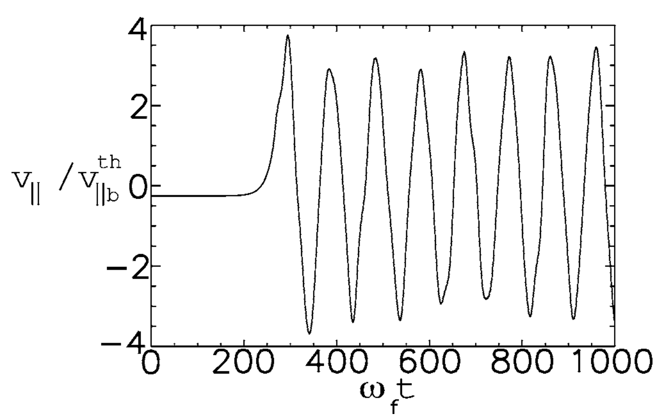

FIG. 11. The normalized parallel velocity $v_\parallel / v_{\parallel b}^{\text{th}}$ of a test particle is plotted as a function of time.

much larger growth rate, $\gamma_{\mathrm{Weibel}}/\gamma_{\mathrm{Harris}} \sim v_{\perp}^{\mathrm{th}}/c \ll 1$. Therefore, the electromagnetic Weibel instability is likely to be an important instability mechanism in relativistic one-component charged particle beams with $\bar{\nu}/\nu_0 > 0.82$, but not in intense beams with $\bar{\nu}/\nu_0 < 0.82$. To study the nonlinear stage of the Weibel instability, the electromagnetic Darwin model has been implemented in the δf particle-in-cell code BEST. The results of the nonlinear simulations show that the nonlinear saturation is governed by longitudinal particle trapping (electrostatic trapping for the Harris instability and electromagnetic trapping for the Weibel instability). Even though in Secs. IV–VI we have chosen the initial longitudinal momentum distribution to be Maxwellian, the conclusions that we have drawn from the simulations remain qualitatively valid for other distributions, as long as one treats the average of the longitudinal kinetic energy spread in the beam frame as the effective longitudinal temperature.

ACKNOWLEDGMENTS

It is a pleasure to acknowledge the benefit of useful discussions with Dr. Wei-li Lee.

This research was supported by the U.S. Department of Energy.

[1]R. C. Davidson and H. Qin, *Physics of Intense Charged Particle Beams in High Energy Accelerators* (World Scientific, Singapore, 2001), and references therein.
[2]M. Reiser, *Theory and Design of Charged Particle Beams* (John Wiley & Sons, New York, 1994).
[3]A. W. Chao, *Physics of Collective Beam Instabilities in High Energy Accelerators* (John Wiley & Sons, New York, 1993).
[4]R. C. Davidson, *Physics of Non-neutral Plasmas* (World Scientific, Singapore, 2001), and references therein.
[5]E. A. Startsev, R. C. Davidson, and H. Qin, Nucl. Instrum. Methods Phys. Res. A **544**, 125 (2005).
[6]E. A. Startsev, R. C. Davidson, and H. Qin, Phys. Rev. ST Accel. Beams **8**, 124201 (2005).
[7]E. A. Startsev, R. C. Davidson, and W. W. Lee, *Proceedings of the 2005 Particle Accelerator Conference* (IEEE, Piscataway, NJ, 2005), p. 3780.
[8]E. A. Startsev, R. C. Davidson, and H. Qin, Phys. Rev. ST Accel. Beams **6**, 084401 (2003).
[9]E. A. Startsev, R. C. Davidson, and H. Qin, Phys. Plasmas **9**, 3138 (2002).
[10]H. Qin, R. C. Davidson, and W. W. Lee, Phys. Rev. ST Accel. Beams **3**, 084401 (2000); **3**, 109901 (2000).
[11]E. A. Startsev, R. C. Davidson, and H. Qin, Laser Part. Beams **20**, 585 (2002).
[12]P. H. Stoltz, R. C. Davidson, and W. W. Lee, Phys. Plasmas **6**, 298 (1999).
[13]H. Qin, R. C. Davidson, W. W. Lee, and E. A. Startsev, *Proceedings of the 2001 Particle Accelerator Conference* (IEEE, Piscataway, NJ, 2001), p. 693.
[14]E. G. Harris, Phys. Rev. Lett. **2**, 34 (1959).
[15]E. A. Startsev and R. C. Davidson, Phys. Plasmas **10**, 4829 (2003).
[16]T.-S. Wang and L. Smith, Part. Accel. **12**, 247 (1982).
[17]T.-S. Wang, Phys. Rev. ST Accel. Beams **7**, 024201 (2004).
[18]A. Friedman, D. A. Callahan, D. P. Grote, A. B. Langdon, and I. Haber, Bull. Am. Phys. Soc. **35**, 2121 (1990).
[19]A. Friedman, R. O. Bangerter, D. A. Callahan, D. P. Grote, A. B. Langdon, and I. Haber, *Proceedings of the 2nd European Particle Accelerator Conference*, Nice, France, 1990, edited by P. A. Martin (Editions Frontieres, Gif-sur-Yvette, France, 1990), Vol 2, p. 1699.
[20]S. M. Lund, D. A. Callahan, A. Friedman, D. P. Grote, I. Haber, and T. F. Wang, *Proceedings of XIX International Linear Accelerator Conference*, Chicago, 1998, edited by C. E. Eyberger, R. C. Pardo, and M. M. White (Argonne National Laboratory, Argonne, IL, 1998), p. 372.
[21]S. M. Lund, J. J. Barnard, G. D. Craig, A. Friedman, D. P. Grote, T. S. Sangster, W. M. Sharp, S. Eylon, T. T. Fessenden, E. Henestroza, S. Yu, and I. Haber, Nucl. Instrum. Methods Phys. Res. A **415**, 345 (1998).
[22]I. Haber, A. Friedman, D. P. Grote, S. M. Lund, and R. A. Kishek, Phys. Plasmas **6**, 2254 (1999).
[23]W. W. Lee, R. C. Davidson, E. A. Startsev, and H. Qin, Nucl. Instrum. Methods Phys. Res. A **544**, 353 (2005).
[24]R. C. Davidson, W. W. Lee, H. Qin, and E. A. Startsev, Phys. Plasmas **9**, 340 (2002).
[25]E. S. Weibel, Phys. Rev. Lett. **2**, 83 (1959).
[26]R. C. Davidson, D. A. Hammer, I. Haber, and C. E. Wagner, Phys. Fluids **15**, 317 (1972).
[27]R. Lee and M. Lampe, Phys. Rev. Lett. **31**, 1390 (1973).
[28]C. A. Kapetanakos, Appl. Phys. Lett. **25**, 484 (1974).
[29]S. E. Parker and W. W. Lee, Phys. Fluids B **5**, 77 (1993).
[30]C. W. Nielson and H. R. Lewis, *Methods in Computational Physics* (Academic, New York, 1976), Vol. 16, p. 976.